Carbon-induced magnetic properties and anomalous Hall effect in Co$_2$Mn$_2$C thin films with $L1_0$-like structures

Shinji Isogami [1,*] Yohei Kota [2] Hideyuki Yasufuku [1] Keiji Oyoshi [1] Masahiko Tanaka,[1] and Yukiko K. Takahashi [1]

[1]*National Institute for Materials Science (NIMS), Sengen 1-2-1, Tsukuba, Ibaraki 305-0047, Japan*
[2]*National Institute of Technology, Fukushima College, Nagao 30, Taira-Kamiarakawa, Iwaki, Fukushima 970–8034, Japan*

Co$_2$Mn$_2$C thin films were synthesized via vacuum carburization of the host CoMn alloy films based on a conventional gas-solid reaction to demonstrate the effect of C, a common light element, on the magnetic and spintronic materials. The crystal structure transitioned from the disordered face-centered-cubic CoMn to the $L1_0$-like Co$_2$Mn$_2$C, for which the lattice constant increased from 0.356 to 0.378 nm. The C 1s x-ray photoemission spectra of the Co$_2$Mn$_2$C film indicated hybridization in C-Co and C-Mn and a homogeneous concentration of C in the film. The enhancement of both the saturation magnetization and the anomalous Hall conductivity (σ_{xy}) was induced by C, attributing to the magnetic transition to the ferrimagnetic spin order. The surface flatness and high σ_{xy} are promising characteristics for spintronic applications such as the spin-anomalous Hall effect. The atom- and spin-resolved density of states (DOS) via first-principles calculations revealed that face-centered Mn(II) and Co could be significantly influenced by C because of p-d hybridization, resulting in enhanced spin polarization of the DOS at the Fermi level of $\sim$0.82. These results demonstrate that the use of C could be an essential way to boost material properties in the future.

I. INTRODUCTION

Material development with various functionalities has attracted considerable attention in terms of material sustainability for next-generation applications. One way to explore this concept is to use an orbital hybridization between metals and light elements with valence electrons of the p state, which has been widely applied to various materials, such as superconductors and semiconductors. For example, the characteristics of MgB$_2$ and SiC comprising light elements are significant owing to their specific orbital hybridization [1,2]. In addition, magnetic and spintronic materials that benefit from this concept are the ferromagnetic and/or ferrimagnetic antiperovskite nitrides, A_3BN (in which N occupies the body-centered site of the face-centered-cubic (fcc) structure formed by A and B, which denote transition metals, e.g., Fe or Mn). This is supported by previously demonstrated effects of these materials, such as the giant inverse tunneling magnetoresistive effect at room temperature [3,4], inverse and efficient current-induced magnetization switching [5–10], anomalous Hall and Nernst effects [11–17], high-speed magnetic domain-wall propagation [18,19], and topological Hall effect in association with skyrmions [20–24]. Even antiferromagnetic nitrides, Mn$_3Y$N (Y = Ni, Cu, Zn, etc.), have been examined because of their predicted intrinsic anomalous Hall effect (AHE) originating from their topological features in electronic structures [25]. These features are associated with the atomic interaction mechanism between metals and N, which has recently engendered an intriguing concept: *material development using 2p-light elements such as B, C, and N* [26,27], making them common alternatives to conventional alloy systems comprising, e.g., expensive elements.

Nitrides have been the most predominantly studied antiperovskite material to date [28–30], whereas carbides have also attracted interest owing to their ability to enhance the characteristics of nitrides. For example, Mehedi *et al.*, Zhang *et al.*, and Tobise *et al.* found that in the co-addition of N and C for $\alpha'' - Fe_{16}(N, C)_2$, namely, C doping acts to suppress the coercivity [31–33]. The magnetic moment and formation energy of Fe$_4X$ (X = B, C, or N) were calculated by Lv *et al.* [34]. The perpendicular magnetic anisotropy could be more enhanced in FeNiC than in FeNiN, as calculated by Kota *et al.* [35]. Tagawa *et al.* predicted a shift in the Fermi level (E_F) without a remarkable change in the total density of states (DOS) of Mn$_4$N$_{1-x}$C$_x$ [36]. These results show that C could potentially satisfy various application requirements, similar to N. Therefore, the thin film fabrication of pure antiperovskite carbides and, subsequently, the elucidation of the role of C, should be the next topics of focus.

The synthesis of single-phase Mn$_4$C is generally difficult because of its low stability [37]. Therefore, Holtzman *et al.* proposed Co as a dopant to improve the stability of the fcc structure [38]. A bulk Co$_2$Mn$_2$C compound was successfully synthesized by induction melting in an inert atmosphere [38]. This demonstration inspired us to fabricate Co$_2$Mn$_2$C thin films and examine their magnetic/spintronic characteristics with a view toward device applications. When light elements such as C contribute to various functionalities, this could serve as a guide for achieving greater material sustainability through the realization of desirable properties without using expensive elements.
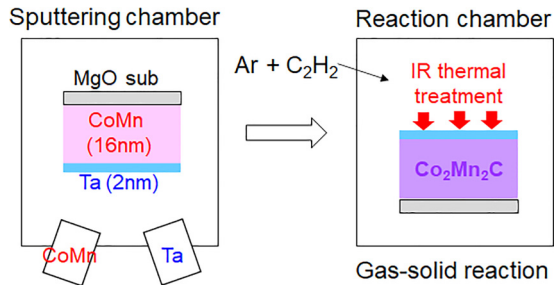
*isogami.shinji@nims.go.jp

FIG. 1. Schematic of the carburization process for the CoMn (16 nm)/Ta (2 nm) thin film.

In this study, a standard gas-solid reaction process in a vacuum was employed to promote the carburization of thin films of the host CoMn alloys, instead of using the conventional co-sputtering of C and CoMn alloy. Consequently, highly atomic-ordered Co_2Mn_2C thin films were successfully formed with a sufficiently flat surface on MgO substrates. Ferromagnetic properties and the AHE were observed in the Co_2Mn_2C thin films at room temperature, indicating their potential as useful spintronic materials. First-principles electronic structure calculations were performed to elucidate the role of C.

II. EXPERIMENT AND COMPUTATIONAL PROCEDURES

Figure 1 shows the preparation of the initial film followed by the carburization process, which is a standard gas-solid reaction. To prepare the initial film, a 16-nm-thick CoMn alloy film was deposited on a single-crystal MgO(100) substrate via magnetron sputtering using a CoMn alloy target at room temperature, which was followed by *in situ* annealing of the film at 350 °C to improve sheet texture formation with the (001) orientation. Notably, the MgO substrate was thermally treated at 600 °C for 1 h to clean the MgO surface, prior to the deposition of the CoMn film. A 2-nm-thick Ta film was deposited as the capping layer at room temperature to protect the CoMn surface from contamination of impurities. The alloy content of the initial film, measured using x-ray fluorescence analysis, was $Co_{51.7}Mn_{48.3}$ (at. %), hereinafter referred to as CoMn.

Vacuum carburization of the initial CoMn film was performed using a mixture of Ar and C_2H_2 gases, in which the flow ratio of C_2H_2 gas was defined as $Q = \frac{C_2H_2}{Ar+C_2H_2}$. The initial film was transferred to a reaction chamber using a hand-carrier box filled with N_2 gas. The Q was controlled using a mass-flow controller while maintaining the total gas pressure at 1 Pa. Focused infrared (IR) was used for thermal treatment (GV154; Thermoriko Corporation, Tokyo, Japan), which can efficiently decrease outgassing from the sample holder made with quartz and/or neighboring vacuum components owing to the selective IR exposure of the CoMn film (together with the MgO substrate). The IR annealing temperature (T_{IR}) and carburization time were optimized to 500 °C and 1 h, respectively. The long-range crystal structures and film-surface morphology were examined using x-ray diffraction (XRD) with Cu-K_α radiation (SmartLab; Rigaku Corporation, Tokyo, Japan) and atomic force microscopy (AFM) (SPA400; SII Nano Technology Inc., Tokyo, Japan),

respectively. X-ray photoemission spectroscopy (XPS) was employed to study the content of C, the chemical interactions between C and Co, as well as between C and Mn (Quantera SXM; ULVAC-PHY, Inc., Kanagawa, Japan). XPS profiles were recorded using Al K_α monochromatic x-rays of 50 W and 200 μm in diameter before and after the Ar ion sputtering of the film surface to assess the depth dependence of C content. The ion sputtering was performed using an ion beam energy of 1 kV on a target area of 2 × 2 mm^2; the reference sputter rate for SiO_2 was maintained at ∼3 nm/min. The binding energy (E_b) was calibrated using both Co and Mn Auger peaks in this XPS analysis because the standard hydrocarbon disappeared by the Ar ion sputtering. The typical content was estimated to be $(Co_{52}Mn_{48})C_{15\pm0.5}$ (at. %) for $Q = 5\%$ and $(Co_{52}Mn_{48})C_{25\pm1}$ (at. %) for $Q = 50\%$. Note that the content of Co and Mn was consistent with that of initial CoMn. The magnetic properties were measured using a vibrating sample magnetometer (VSM 8600 series; Lake Shore Cryotronics, Inc., Ohio, USA). The transverse resistivity (ρ_{xy}) was measured using a physical property measurement system (Dynacool; Quantum Design Inc., CA, USA) to examine the AHE.

The detail of the calculation is the same as in our previous study [35], using the Vienna ab-initio simulation package (VASP) [39,40]. The generalized gradient approximation parametrized by Perdew–Burke-Ernzerhof [41] was adopted to deal with the exchange-correlation functional. The magnetic anisotropy energy was evaluated from the energy difference when the magnetization aligns along the a- and c directions, $\Delta E = E_a - E_c$, based on the magnetic force theorem using the energy including spin-orbit interaction. The cutoff energy of the plane-wave basis was 520 eV, and the k-point mesh for sampling was set to 11 × 11 × 11 in the Brillouin zone.

III. RESULTS AND DISCUSSION

A. Characterization of the Co_2Mn_2C crystal structures

Figure 2(a) shows the out-of-plane XRD profiles of the films with various Q in the carburization process. For both the initial CoMn film and the film with carburization process in pure Ar gas ($Q = 0\%$), a diffraction peak originating from CoMn(002) was observed at only $2\theta/\omega \approx 51°$, suggesting the existence of a disordered fcc structure of CoMn with a lattice constant of 0.356 nm. In contrast, new diffraction peaks appeared at $2\theta/\omega \approx 23.4°$ and 47.9° for the films with $Q > 5\%$, suggesting a structural transition with a lattice constant of 0.378 nm, which is close to that of the antiperovskite Mn_4N [42]. In order to identify the compound, we first calculated the XRD patterns for the Co_2Mn_2C unit cell that is proposed by Holtzman *et al.* as one of the candidates [38]. It was revealed that the peaks at $2\theta/\omega \approx 23.4°$ and 47.9° could be attributed to the superlattice and fundamental lattice of the Co_2Mn_2C, respectively. In addition, the XRD patterns for the unit cell without C were calculated to distinguish the degree of order for C atom from that for Co and Mn atoms. The superlattice peak appeared for both films, the Co_2Mn_2C and the film without C, because of the layer-by-layer ordering of Co and Mn monolayers along the
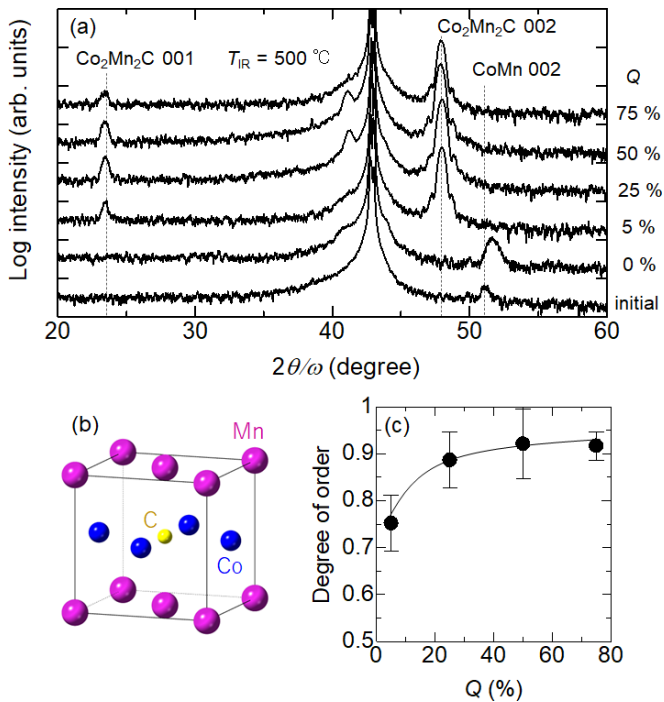
FIG. 2. (a) Out-of-plane XRD profiles of the CoMn (16 nm)/Ta (2 nm) thin films carburized at various C_2H_2 gas flow ratios relative to that of the Ar + C_2H_2 gas mixture (Q), where the IR thermal treatment temperature (T_{IR}) was 500 °C. (b) Possible crystal structure of Co_2Mn_2C formed by carburization with $Q > 5\%$. (c) Degree of atomic order of Co_2Mn_2C crystals as a function of Q.

FIG. 3. (a) Photograph of the initial CoMn (16 nm)/Ta (2 nm) (left) and the carburized Co_2Mn_2C (16 nm)/Ta (2 nm) (right). Atomic force microscopy images of (b) the initial and (c) the carburized surfaces.

direction perpendicular to the film plane, which is similar to the $L1_0$-type FePt alloy. However, quantification of the XRD intensity of the superlattice and fundamental peaks allowed us to conclude that the dominant phase after carburization is Co_2Mn_2C, as shown in Fig. 2(b) (Sec. S1 in Supplemental Material [43]). Note that the preferential site of the C atom is the body center of the unit cell, similar to the N atom in antiperovskite nitrides, such as Fe_4N and/or Mn_4N. The threshold T_{IR} to form the Co_2Mn_2C was approximately 500 °C, and the carburization mechanism was examined using an initial film of CoMn with thicker Ta capping layer (Sec. S2 in Supplemental Material [43]). Figure 2(c) shows the entire degree of order of Co, Mn, and C as a function of Q, calculated using a method described in literature [14,16]. A low degree of order was observed at $Q < 25\%$; it increased with increasing Q and saturated at ∼0.92, indicating the desorption of excess C at high-Q values. Therefore, the amount of C embedded in the unit cell should be determined by the number of preferential sites of C. Notably, carburization is not applicable only for CoMn alloy films because the formability should be governed by the phase stability of carbides. For example, the partial substitution of C for N is possible regardless of the instability of pure carbides, as in the case of $\alpha'' - Fe_{16}(N, C)_2$ [31–33].

Figure 3(a) shows photographs of the initial CoMn (left) and carburized Co_2Mn_2C thin films (right). The color of both films was metallic with similar transparency, suggesting no remarkable change in the film thickness. This is supported by the x-ray reflection measurements of the two films
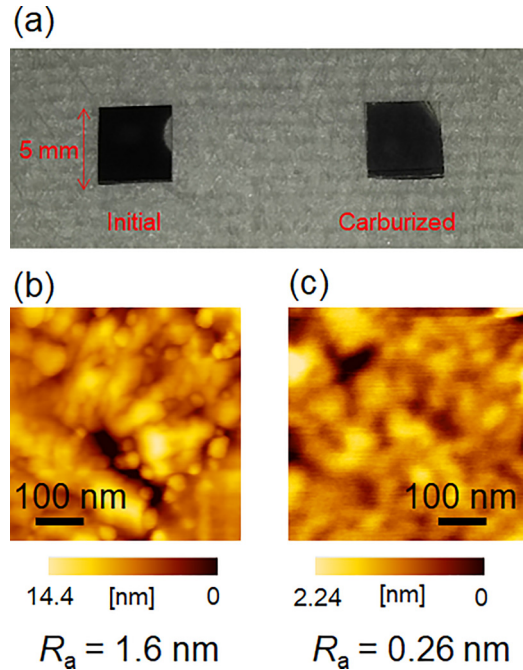
(Sec. S3 in Supplemental Material [43]). Figures 3(b) and 3(c) show the AFM images of the initial CoMn and the carburized Co_2Mn_2C thin films, respectively. The surface roughness (R_a) of the Co_2Mn_2C film was one order of magnitude smaller than that of the CoMn film, which can be attributed to the higher degree of order of the Co_2Mn_2C crystal compared to that of the disordered CoMn.

B. XPS analysis of Co, Mn, and C

To confirm the chemical interactions for the C-Co and C-Mn, and the compositional gradient of C along the film normal, XPS analysis was conducted. Figures 4(a) and 4(b) show the Co $2p$ and Mn $2p$ spectra, respectively, for the CoMn, Co_2Mn_2C, and pure Co and Mn thin films. The E_b values of the Co_2Mn_2C and CoMn spectra were calibrated with respect to those of the Auger peaks of pure Co and Mn, because the peak of hydrocarbon at the top surface that is employed for a standard calibration is removed by Ar ion sputtering to assess the inner part of films in this measurement. Although the calibration method is unusual, it was also true that we could not find any deviation of the E_b for three Co and Mn Auger spectra [insets of Figs. 4(a) and 4(b)], resulting in unnecessity of calibration itself. Contrary to our expectations, no remarkable chemical shift of the major peaks was observed in the doublet peaks of Co $2p$ and Mn $2p$, compared with those of the pure Co and Mn reference films. Figure 4(c) shows the C $1s$ spectra of the CoMn film before and after Ar ion sputtering for 4 min, corresponding to the inner part of the film from the top surface. The peak at $E_b \approx 284.8$ eV originates from hydrocarbons on the CoMn film surface, judging from the fact that the peak vanished after
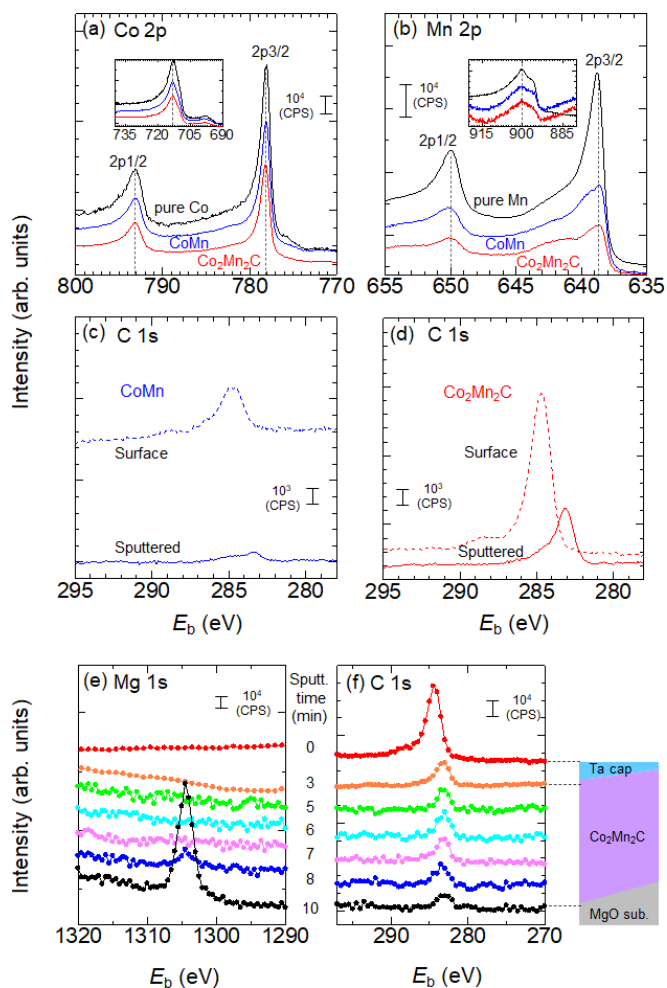
FIG. 4. XPS spectra for (a) Co 2p, (b) Mn 2p, and (c), (d) C 1s edges measured before and after Ar ion sputtering. The blue, red, and black lines represent the peaks of CoMn, Co$_2$Mn$_2$C, and pure Co or Mn films as reference samples, respectively. XPS spectra for the film surfaces are depicted by dashed lines [Figs. 4(c) and 4(d)]. The insets of Figs. 4(a) and 4(b) show the Auger peaks of Co and Mn, respectively, used for calibration of E_b. Sputtering time-dependent XPS spectra of (e) Mg 1s and (f) C 1s.

FIG. 5. In-plane (//) and out-of-plane ($\perp$) magnetization hysteresis loops for (a1), (a2) CoMn film with $Q = 0\%$ and (b1), (b2) Co$_2$Mn$_2$C film with $Q = 50\%$, measured at 4 and 300 K. (c) Temperature dependence of magnetization (*M-T* curves) for both films.

Ar ion sputtering. In contrast to the spectrum of the initial CoMn film, a clear peak appeared even after Ar ion sputtering at $E_b \approx 283$ eV for the Co$_2$Mn$_2$C film [Fig. 4(d)], and the chemical shift was estimated to be ~ -1.8 eV with respect to the peak corresponding to the hydrocarbons. This might be explained by the hybridization with light element of C, in contrast to the general case of metal-based hybridization. The chemical shift akin to that observed in the C 1s spectrum toward a lower E_b is also observed, for example, in the case of TiC, for which $E_b \approx 281.5$ eV [44]. This might be related to the enhanced charge density around C, as predicted by first-principles calculations [34]. These XPS results conclude that the carburization of the CoMn alloy thin film promoted the hybridization in C-Co and C-Mn, resulting in the formation of Co$_2$Mn$_2$C. Figures 4(e) and 4(f) show the sputtering time-dependent depth profiles of the Mg 1s and C 1s spectra, respectively. The strongest C 1s peak was observed at $E_b \approx 284.8$ eV, corresponding to the hydrocarbon on top
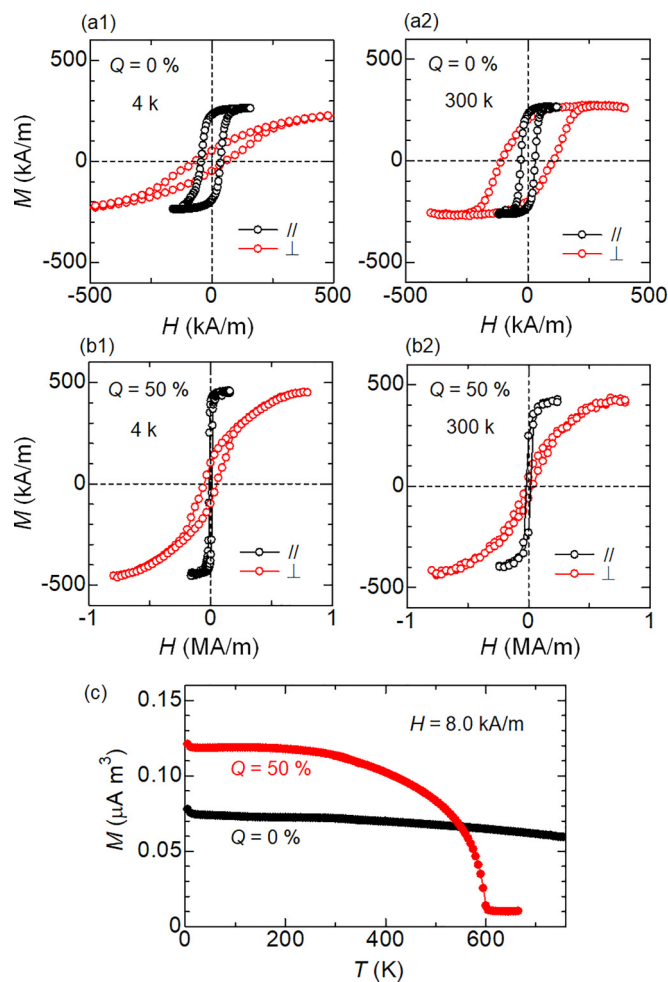
as shown by dashed line of Fig. 4(d). After sputtering for 3 min, the peak intensity of C 1s did not change until the MgO surface appeared with sputtering for longer than 8 min. The results indicate the uniform concentration of C along the Co$_2$Mn$_2$C film normal, as shown in the schematic on the right. Given that the carburization occurs via diffusion of C from top to bottom (Sec. S2 in Supplemental Material [43]), a compositional gradient may occur in the Co$_2$Mn$_2$C layer. However, the film thickness of 16 nm in this study might be sufficiently thin to eliminate such a C gradient.

C. C-induced magnetic properties

Figures 5(a1) and 5(a2) show the magnetization hysteresis (*M-H*) loops at 4 and 300 K, respectively, for the disordered CoMn film carburized with $Q = 0\%$. The saturation magnetization (M_s) was ~ 300 kA/m, and the magnetic anisotropy was observed with the easy axis pointing in the in-plane (//) direction at 4 K. The magnetic field at which magnetic saturation occurs along the out-of-plane direction ($\perp$) was smaller at 300 K than that at 4 K, suggesting a decrease in in-plane magnetic anisotropy at 300 K. Figures 5(b1) and 5(b2)
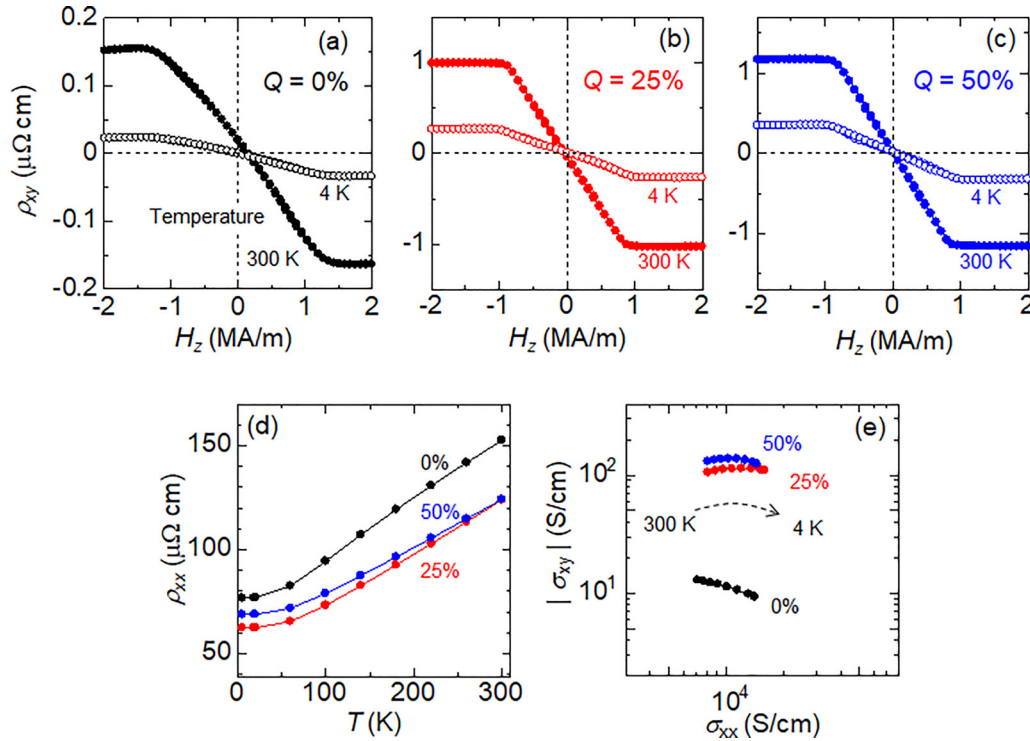
FIG. 6. (a)–(c) Transverse resistivity (ρ_{xy}) as a function of applied magnetic field along the film normal (H_z) for the CoMn film with $Q = 0\%$, and the Co_2Mn_2C film with $Q = 25$ and 50%. (d) Longitudinal resistivity (ρ_{xx}) as a function of measurement temperature (T) for all films. (e) Transverse conductivity ($|\sigma_{xy}|$) as a function of the longitudinal conductivity (σ_{xx}).

show the *M-H* loops at 4 and 300 K, respectively, for the highly ordered Co_2Mn_2C film carburized with $Q = 50\%$. Two remarkable characteristics were observed: (1) the in-plane magnetic anisotropy was almost independent of the measurement temperature, 4 and 300 K; (2) the M_s was ~1.7 times higher for $Q = 50\%$ than that for $Q = 0\%$. Figure 5(c) shows the temperature (T) dependence of M (*M-T* curve) under the applied field of 8.0 kA/m in the in-plane direction, in which field cooling was applied with 200 kA/m in the in-plane direction. The Curie temperature (T_c) was approximately 600 K for $Q = 50\%$, whereas a clear T_c was not observed for $Q = 0\%$. These can be attributed to the different magnetic structures. Although it is not clear that the different magnetic structures for $Q = 0\%$ might be related to the disordered crystal structure [Fig. 2(c)], the collinear ferromagnetic and/or ferrimagnetic structure might be stable with $Q = 50\%$ [38].

D. C-induced enhancement of anomalous Hall properties

Figures 6(a)–6(c) show the ρ_{xy} as a function of the external magnetic field along the film normal (H_z), which is given by, $\rho_{xy} = R_0(\mu_0 H_z) + R_{AH}M$, where $R_{0(AH)}$ represents the normal Hall (anomalous Hall) coefficient. The normal Hall component can be eliminated by fitting to the ρ_{xy}-H_z hysteresis loop. Consequently, the ρ_{xy} in Figs. 6(a)–6(c) directly indicates the AHE component for three samples. The smallest saturation AHE was observed for $Q = 0\%$, which increased with increasing Q. The hysteresis of AHE was found similar to the *M-H* loops measured in $\perp$ directions [Figs. 5(b1) and 5(b2)]. However, a large discrepancy was found for $Q = 0\%$. In particular, the magnetic coercivity (H_c) observed in the *M-*

H loop disappeared in the AHE, which may be attributed to the superposition of topological Hall components caused by the non-collinear magnetic configurations [20–24]. To consider this speculation, we additionally measured the magnetoresistive (MR) effect in perpendicular geometry, that is, the longitudinal resistivity (ρ_{xx}) was recorded as a function of H_z (ρ_{xx}-H_z hysteresis loop) (Sec. S4 in Supplemental Material [43]). Note that some steplike behaviors were observed for the ρ_{xx}-H_z loop, suggesting the presence of non-collinear magnetic configuration as indicated by some reports [45,46]. Figure 6(d) shows the ρ_{xx} as a function of T, indicating metallic conduction in all films. Figure 6(e) shows the relationship between the transverse conductivity ($|\sigma_{xy}|$), defined as $\sigma_{xy} = -\frac{\rho_{xy}}{\rho_{xy}^2 + \rho_{xx}^2}$, and longitudinal conductivity (σ_{xx}). The σ_{xy} was nearly constant when $\sigma_{xx} \approx 10^4$ S/cm for $Q = 25$ and 50%, suggesting that the intrinsic mechanism can dominate the AHE and that the quality of the crystal is moderate [47,48]. Furthermore, the measured value, $|\sigma_{xy}| \approx 100$ S/cm, was within the range of 100–1000 S/cm, which is typically observed in conventional pure ferromagnets and their alloys, such as Fe [49] and Fe–Ga [49], and even in Heusler alloys, such as $Co_2Mn(Al, Si)$ [50]; however, the value is higher than that in antiperovskite ferrimagnetic nitrides, such as Mn_4N ($|\sigma_{xy}| \approx 80$ S/cm) [16]. The $|\sigma_{xy}|$ for $Q = 0\%$ was one order of magnitude smaller than that for $Q = 25$ and 50% and decreased with decreasing T. Therefore, the AHE mechanism for $Q = 0\%$ is contaminated by the extrinsic mechanism. In addition, the enhanced AHE for $Q = 25$ and 50% is associated with the C ordered at the body site of the $L1_0$-like CoMn unit cell.
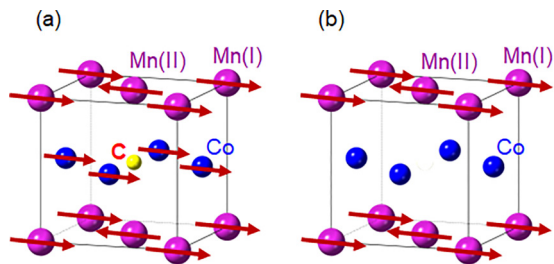
FIG. 7. (a) Schematics of the Co_2Mn_2C unit cell together with the stable magnetic structures predicted by first-principles calculations. (b) Same model as (a) without C atoms for the comparison purpose.

E. C-induced magnetic and electronic structures

To discuss the effect of C on the magnetic and AHE properties of the Co_2Mn_2C thin films, the magnetic moment and atom-resolved DOS were examined via the first-principles electronic structure calculations using the Vienna *Ab initio* Simulation Package [39,40]. Figure 7(a) shows the stable crystal and magnetic structures of the Co_2Mn_2C model unit cell based on our calculation in which Mn(I) and Mn(II) correspond to Mn atoms ordered at corner- and face-centered sites, respectively. We have considered some possible magnetic structures with ferromagnetic, ferrimagnetic, and antiferromagnetic states as initial conditions, however, the result of the self-consistent electronic structure calculation converged to the magnetic structure shown in Fig. 7(a) or higher energy states. These results show that the magnetic structure modeled in Fig. 7(a) should be energetically local minimum for the Co_2Mn_2C. One can find that our magnetic model is consistent with the previous study given by Holtzman *et al.* [38]. Note that the formation energy of Co_2Mn_2C was predicted to be -0.366 eV/f.u., indicating much higher stability compared with the other carbides such as Fe_2Ni_2C ($0.137 \sim 0.266$ eV/f.u.) and Fe_2Co_2C ($0.038 \sim 0.162$ eV/f.u.) calculated by the same procedure [35]. The calculated equilibrium lattice constants of the Co_2Mn_2C model unit cell were $a = 0.374$ nm and $c = 0.383$ nm, which agree well with the experimental result ($a \approx c \approx 0.378$ nm).

The in-plane magnetic anisotropy of the Co_2Mn_2C model was found similar to the experimental observations [Fig. 5(b)]. The magnetic anisotropy energy was calculated to be -1.8 MJ/m^3, suggesting that the magnetization easy-axis aligns along the in-plane direction. To elicit the effect of C, a CoMn unit cell without C atoms [Fig. 7(b)] was modeled using the equilibrium lattice constants of Co_2Mn_2C. Table I lists the magnetic moment per atom. The magnetic moment

TABLE I. Calculated magnetic moment and comparison with experiments.

	Mn(I) (μ_B/atom)	Mn(II) (μ_B/atom)	Co (μ_B/atom)	M_s (μ_B/f.u.)	$M_s^{exp.(4K)}$ (μ_B/f.u.)
Co_2Mn_2C	3.78	-2.26	0.19	2.00	2.82
CoMn	3.31	-3.31	0	0	1.44

of Mn(I) was larger than that of Mn(II) but with the opposite sign, and that of Co was remarkably small, resulting in overall $M_s = 2.00$ μ_B/f.u. for the Co_2Mn_2C unit cell. The low magnetic moment at the face-centered Mn(II) was caused by a stronger hybridization between the Mn $3d$ and C $2p$ orbitals owing to their smaller interatomic distance than that with the corner Mn(I), which is consistent with a conventional Mn_4N unit cell [42]. M_s observed in the experiments at 4 K was larger (by $\sim40\%$) than the calculated one. This discrepancy can be related to the deterioration in the magnetic structure of the stoichiometric Co_2Mn_2C [Fig. 7(a)] because of the imperfect degree of order as shown in Fig. 2(c). The total M_s was calculated to be 0 for the CoMn film without C, suggesting the antiferromagnetic nature of CoMn when ordered in the $L1_0$ type [Fig. 7(b)]. The results are consistent with those of a previous study [51], in which CoMn formed an antiferromagnet with Mn content greater than 43 at. %. Conversely, experimental results indicated a high $M_s \sim 1.44$ μ_B/f.u. at 4 K. This is related to the disordered fcc structure of the fabricated initial CoMn film, which was confirmed by XRD analysis where no peak was observed to originate from the superlattice structure at $2\theta/\omega \approx 23°$ [Fig. 2(a)]. Such an atomic disorder caused an imperfect magnetic compensation between Co and Mn, resulting in high M_s in the experiment.

Figures 8(a)–8(c) show the atom-resolved DOS for each electron spin in the $3d$ state. For Mn(I), a slight change in the DOS was observed for Co_2Mn_2C (depicted by the red line) compared to that for CoMn (depicted by the blue line). In contrast, the changes in the DOS were tangible for Mn(II) and Co; the large unoccupied states for both up and down spins near $E - E_F \approx 1$ eV decreased and shifted toward the low-energy direction. These results suggest a dominating influence of C on the DOS of face-centered atoms, such as in Mn(II) and Co, because of the presence of nearest-neighbor sites, compared with corner atoms, such as in Mn(I). To examine a possible *p-d* hybridization, the DOS of C in the $2p$ state was considered [Fig. 8(d)]. A large and relatively broad state can be observed near $E - E_F \approx 5$ eV, which might be responsible for the low-energy shift of the DOS for Mn(II) and Co because of *p-d* hybridization. Figure 8(e) shows the total DOS of the antiferromagnetic CoMn and ferrimagnetic Co_2Mn_2C. The C causes a shift in the total DOS for Co_2Mn_2C, resulting in enhanced spin polarization (P) of the DOS at the E_F. P was estimated to be ~0.82 [inset of Fig. 8(e)], which is smaller than that of Heusler alloy systems with half metallicity ($P \approx 1$) at low temperatures; however, it is larger than or comparable to that of the family of antiperovskite materials, such as Mn_4N ($P \approx 0.44$) [15], Fe_4N ($P \approx -0.6$) [15,52], Co_4N ($P \approx -0.86$) [53], and Ni_4N ($P \approx -0.2$) [53], as well as conventional ferromagnets, such as CoFe ($P \approx 0.6$) [54], Fe ($P \approx 0.5$) [54], and Co ($P \approx 0.45$) [54]. The enhanced P caused by C is consistent with the case of N [52], suggesting a universal effect for $2p$-light elements [26].

In recent years, the AHE has been demonstrated as a potential source of spin current to achieve current-induced magnetization switching, referred to as the spin AHE (SAHE) [55,56]. Since an enhanced SAHE is responsible for higher switching efficiency, developing technologies to promote the SAHE has been the focus of research in SAHE-based switching devices [57]. Trilayered structures comprising
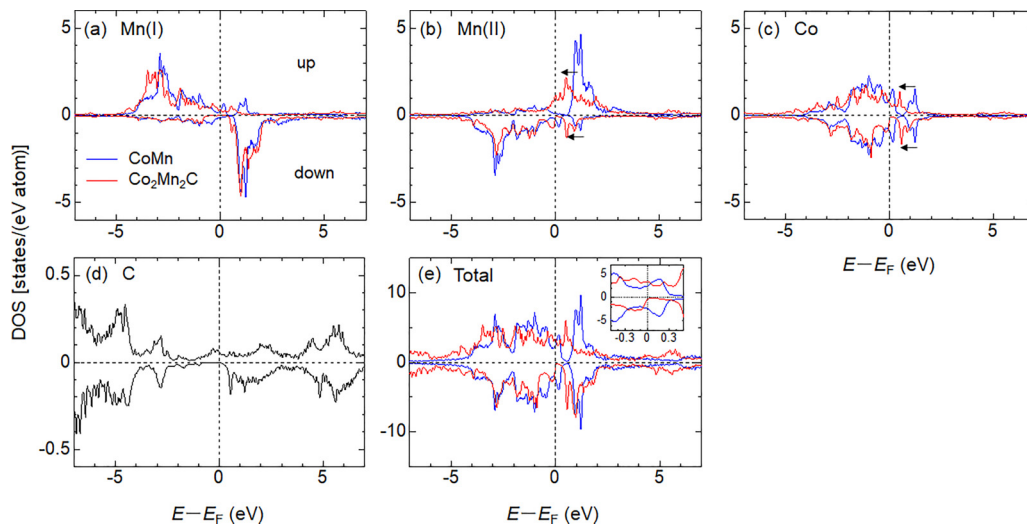
FIG. 8. Atom- and spin-resolved DOS for the $3d$ states of (a) Mn(I), (b) Mn(II), (c) Co, and (d) the $2p$ states of C. (e) Total DOS for the CoMn and Co_2Mn_2C.

FM1/NM/FM2 are fabricated, where the FM1 is either ferromagnetic or ferrimagnetic layer for the source of spin current via the SAHE, FM2 is a switching layer, and NM is a nonmagnetic layer that separates the FM1 and FM2 layers [58–61]. Furthermore, in-plane magnetic anisotropy is essential for the FM1 to provide an efficient torque to the FM2. Therefore, the FM1 with the help of C such as Co_2Mn_2C thin film, involving enhanced thin film characteristics such as in-plane magnetic anisotropy and high AHE, may be useful for device applications.

IV. CONCLUSION

Ferrimagnetic Co_2Mn_2C thin films were fabricated via vacuum carburization of host CoMn alloy films based on a conventional gas-solid reaction with an Ar and C_2H_2 gas mixture. The carburization process led to (i) transition of the crystal structure from the disordered fcc to the $L1_0$-like structure with a degree of order as large as 0.82, (ii) lattice expansion from 0.356 to 0.387 nm, (iii) occurrence of ferrimagnetic order with in-plane magnetic anisotropy, and (iv) enhancement of M_s and σ_{xy} as well as P compared with the conventional ferromagnets. The observations were supported by first-principles electronic structure calculations. The face-centered Mn(II) and Co were predominantly influenced by C because of p-d hybridization, resulting in enhanced spin polarization of DOS at an E_F of ∼0.82. The smooth surface of $R_a \approx 0.26$ nm and the relatively high AHE could have potential for applications such as SAHE-based switching devices.

[1] J. Nagamatsu, N. Nakagawa, T. Muranaka, Y. Zenitani, and J. Akimitsu, Superconductivity at 39 K in magnesium diboride, Nature (London) **410**, 63 (2001).

[2] M. Bhatnagar and B. J. Baliga, Comparison of 6H-SiC, 3C-SiC, and Si for power devices, IEEE Trans. Electr. Dev. **40**, 645 (1993).

[3] K. Sunaga, M. Tsunoda, K. Komagaki, Y. Uehara, and M. Takahashi, Inverse tunnel magnetoresistance in magnetic tunnel junctions with an Fe_4N electrode, J. Appl. Phys. **102**, 013917 (2007).

[4] Y. Komasaki, M. Tsunoda, S. Isogami, and M. Takahashi, 75% inverse magnetoresistance at room temperature in Fe_4N/MgO/CoFeB magnetic tunnel junctions fabricated on Cu underlayer, J. Appl. Phys. **105**, 07C928 (2009).

[5] S. Isogami, M. Tsunoda, Y. Komasaki, A. Sakuma, and M. Takahashi, Inverse current-induced magnetization switching in magnetic tunnel junctions with Fe_4N free layer, Appl. Phys. Express **3**, 103002 (2010).

[6] T. Hajiri, S. Ishino, K. Matsuura, and H. Asano, Electrical current switching of the noncollinear antiferromagnet Mn_3GaN, Appl. Phys. Lett. **115**, 052403 (2019).

[7] H. Li, G. Wang, D. Li, P. Hu, W. Zhou, X. Ma, S. Dang, S. Kang, T. Dai, F. Yu, X. Zhou, S. Wu, and S. Li, Spin-orbit torque-induced magnetization switching in epitaxial Au/Fe_4N bilayer films, Appl. Phys. Lett. **114**, 092402 (2019).

[8] H. Li, G. Wang, D. Li, P. Hu, W. Zhou, S. Dang, X. Ma, T. Dai, S. Kang, F. Yu, X. Zhou, S. Wu, and S. Li, Field-Free deterministic magnetization switching with ultralow current density in epitaxial Au/Fe_4N bilayer films, ACS Appl. Mater. Interfaces **11**, 16965 (2019).

[9] H. Bai, T. Xu, Y. Dong, H. Zhou, and W. Jiang, Spin-torque switching in rare-earth-free compensated

ferrimagnet Mn$_4$N films, Adv. Electron. Mater. **8**, 2100772 (2021).

[10] S. Isogami, N. Rajamanickam, Y. Kozuka, and Y. K. Takahashi, Efficient current-driven magnetization switching owing to isotropic magnetism in a highly symmetric 111-oriented Mn$_4$N epitaxial single layer, AIP Adv. **11**, 105314 (2021).

[11] Y. Zhang, W. B. Mi, X. C. Wang, and X. X. Zhang, Scaling of anomalous Hall effects in facing-target reactively sputtered Fe$_4$N films, Phys. Chem. Chem. Phys. **17**, 15435 (2015).

[12] K. Kabara, M. Tsunoda, and S. Kokado, Anomalous Hall effects in pseudo-single-crystal γ'-Fe$_4$N thin films, AIP Adv. **6**, 055801 (2016).

[13] S. Isogami, K. Takanashi, and M. Mizuguchi, Dependence of anomalous Nernst effect on crystal orientation in highly ordered γ'-Fe$_4$N films with anti-perovskite structure, Appl. Phys. Express **10**, 073005 (2017).

[14] S. Isogami, A. Anzai, T. Gushi, T. Komori, and T. Suemasu, Temperature independent, wide modulation of anomalous Hall effect by Mn doping in Fe$_{4-x}$Mn$_x$N pseudo-single-crystal films, Jpn. J. Appl. Phys. **57**, 120305 (2018).

[15] A. Anzai, T. Gushi, T. Komori, S. Honda, S. Isogami, and T. Suemasu, Transition from minority to majority spin transport in iron-manganese nitride Fe$_{4-x}$Mn$_x$N films with increasing x, J. Appl. Phys. **124**, 123905 (2018).

[16] S. Isogami, K. Masuda, Y. Miura, N. Rajamanickam, and Y. Sakuraba, Anomalous Hall and Nernst effects in ferrimagnetic Mn$_4$N films: Possible interpretations and prospects for enhancement, Appl. Phys. Lett. **118**, 092407 (2021).

[17] Z. Zhang, X. Shi, X. Liu, X. Chen, and W. Mi, Microstructure, magnetic and electronic transport properties of reactively facing-target sputtered epitaxial Mn$_4$N films, J. Phys.: Condens. Matter. **34**, 065802 (2022).

[18] T. Gushi, M. J. Klug, J. P. Garcia, S. Ghosh, J. P. Attané, H. Okuno, O. Fruchart, J. Vogel, T. Suemasu, S. Pizzini, and L. Vila, Large current driven domain wall mobility and gate tuning of coercivity in ferrimagnetic Mn$_4$N thin films, Nano Lett. **19**, 8716 (2019).

[19] S. Ghosh, T. Komori, A. Hallal, J. P. Garcia, T. Gushi, T. Hirose, H. Mitarai, H. Okuno, J. Vogel, M. Chshiev, J. P. Attané, L. Vila, T. Suemasu, and S. Pizzin, Current-driven domain wall dynamics in ferrimagnetic nickel-doped Mn$_4$N Films: Very large domain wall velocities and reversal of motion direction across the magnetic compensation point, Nano Lett. **21**, 2580 (2021).

[20] C. T. Ma, T. Q. Hartnett, W. Zhou, P. V. Balachandran, and S. J. Poon, Tunable magnetic skyrmions in ferrimagnetic Mn$_4$N, Appl. Phys. Lett. **119**, 192406 (2021).

[21] T. Bayaraa, C. Xu, and L. Bellaiche, Magnetization Compensation Temperature and Frustration-Induced Topological Defects in Ferrimagnetic Antiperovskite Mn$_4$N, Phys. Rev. Lett. **127**, 217204 (2021).

[22] S. Isogami, M. Ohtake, and Y. K. Takahashi, Impact of B-doping on topological Hall resistivity in (111)- and (110)-oriented Mn$_4$N single layers with the non-collinear spin structure, J. Appl. Phys. **131**, 073904 (2022).

[23] G. Wang, S. Wu, W. Zhou, H. Li, D. Li, T. Dai, S. Kang, S. Dang, X. Ma, P. Hu, and S. Li, Ferroelectric polarization control of spin states in Mn$_4$N/PMN-PT heterostructures revealed by topological Hall effect, Appl. Phys. Lett. **113**, 122403 (2018).

[24] M. Meng, S. Li, M. Saghayezhian, E. W. Plummer, and R. Jin, Observation of large exchange bias and topological Hall effect in manganese nitride films, Appl. Phys. Lett. **112**, 132402 (2018).

[25] V. Thi Ngoc Huyen, M.-T. Suzuki, K. Yamauchi, and T. Oguchi, Topology analysis for anomalous Hall effect in the noncollinear antiferromagnetic states of Mn$_3$AN (A = Ni, Cu, Zn, Ga, Ge, Pd, In, Sn, Ir, Pt), Phys. Rev. B **100**, 094426 (2019).

[26] S. Isogami and Y. K. Takahashi, Antiperovskite magnetic materials with $2p$ light elements for future practical applications, Adv. Electron. Mater. **9**, 2200515 (2023).

[27] J. Cui, M. Kramer, L. Zhou, F. Liu, A. Gabay, G. Hadjipanayis, B. Balasubramanian, and D. Sellmyer, Current progress and future challenges in rare-earth-free permanent magnets, Acta Mater. **158**, 118 (2018).

[28] K. Ito, S. Honda, and T. Suemasu, Transition metal nitrides and their mixed crystals for spintronics, Nanotechnology **33**, 062001 (2022).

[29] Z. Zhang and W. Mi, Progress in ferrimagnetic Mn$_4$N films and its heterostructures for spintronics applications, J. Phys. D: Appl. Phys. **55**, 013001 (2022).

[30] J. M. D. Coey, D. Givord, and D. Fruchart, Metallic nitride and carbide Perovskites: History and prospects, ECS J. Solid State Sci. Technol. **11**, 055002 (2022).

[31] M. Mehedi, Y. Jiang, P. K. Suri, D. J. Flannigan, and J. P. Wang, Minnealloy: a new magnetic material with high saturation flux density and low magnetic anisotropy, J. Phys. D: Appl. Phys. **50**, 37LT01 (2017).

[32] X. Zhang and J. P. Wang, High saturation magnetization and low magnetic anisotropy Fe-CN martensite thin film, Appl. Phys. Lett. **114**, 152401 (2019).

[33] M. Tobise, Y. Nomura, M. Kodama, T. Murakami, and S. Saito, Proposal of new co-addition method for α''-Fe$_{16}$(N,C)$_2$ particles by gas-solid reactions, IEEE Trans. Magn. **58**, 2000805 (2022).

[34] Z. Q. Lv, Y. Gao, S. H. Sun, M. G. Qv, Z. H. Wang, Z. P. Shi, and W. T. Fu, Electronic, magnetic and elastic properties of γ-Fe$_4$X (X=B/C/N) from density functional theory calculations, J. Magn. Magn. Mater. **333**, 39 (2013).

[35] Y. Kota and A. Sakuma, First-principles prediction of magnetic properties in Fe(Co,Ni)(C,N)$_{0.5}$ alloys, Appl. Phys. Lett. **120**, 132405 (2022).

[36] Y. Tagawa and K. Motizuki, Electronic band structures and magnetism of intermetallic manganese compounds Mn$_4$X (X identical to N, C), J. Phys.: Condens. Matter. **3**, 1753 (1991).

[37] P. Z. Si, H. D. Qian, H. L. Ge, J. Park, and C. J. Choi, Enhancing the magnetization of Mn$_4$C by heating, Appl. Phys. Lett. **112**, 192407 (2018).

[38] A. H. Holtzman and G. P. Conrad, Structural and magnetic properties of Mn-Co-C alloys, J. Appl. Phys. **30**, S103 (1959).

[39] G. Kresse and J. Hafner, *Ab initio* molecular dynamics for liquid metals, Phys. Rev. B **47**, 558 (1993).

[40] G. Kresse and J. Furthmuller, Efficient iterative schemes for *ab initio* total-energy calculations using a plane-wave basis set, Phys. Rev. B **54**, 11169 (1996).

[41] J. P. Perdew, K. Burke, and M. Ernzerhof, Generalized Gradient Approximation Made Simple, Phys. Rev. Lett. **77**, 3865 (1996).

[42] S. Isogami, K. Masuda, and Y. Miura, Contributions of magnetic structure and nitrogen to perpendicular magnetocrystalline anisotropy in antiperovskite ε-Mn$_4$N, Phys. Rev. Mater. **4**, 014406 (2020).

[43] See Supplemental Material at http://link.aps.org/supplemental/10.1103/PhysRevMaterials.7.014411 for the crystal structure and principles of carburization for Co_2Mn_2C thin films.

[44] L. I. Johansson, H. I. P. Johansson, and K. L. Hakansson, Surface-shifted N 1s and C 1s levels on the (100) surface of TiN and TiC, Phys. Rev. B **48**, 14520 (1993).

[45] H. Du, D. Liang C. Jin, L. Kong, M. J. Stolt, W. Ning, J. Yang, Y. Xing, J. Wang, R. Che, J. Zang, S. Jin, Y. Zhang, and M. Tian, Electrical probing of field-driven cascading quantized transitions of skyrmion cluster states in MnSi nanowires, Nat. Commun. **6**, 7637 (2015).

[46] C. Hanneken, F. Otte, A. Kubetzka, B. Dupé, N. Romming, K. von Bergmann, R. Wiesendanger, and S. Heinze, Electrical detection of magnetic skyrmions by tunnelling non-collinear magnetoresistance, Nat. Nanotechnol. **10**, 1039 (2015).

[47] S. Onoda, N. Sugimoto, and N. Nagaosa, Quantum transport theory of anomalous electric, thermoelectric, and thermal Hall effects in ferromagnets, Phys. Rev. B **77**, 165103 (2008).

[48] N. Nagaosa, J. Sinova, S. Onoda, A. H. MacDonald, and N. P. Ong, Anomalous Hall effect, Rev. Mod. Phys. **82**, 1539 (2010).

[49] H. Nakayama, K. Masuda, J. Wang, A. Miura, K.-I. Uchida, M. Murata, and Y. Sakuraba, Mechanism of strong enhancement of anomalous Nernst effect in Fe by Ga substitution, Phys. Rev. Mater. **3**, 114412 (2019).

[50] Y. Sakuraba, K. Hyodo, A. Sakuma, and S. Mitani, Giant anomalous Nernst effect in the $Co_2MnAl_{1-x}Si_x$ Heusler alloy induced by Fermi level tuning and atomic ordering, Phys. Rev. B **101**, 134407 (2020).

[51] J. W. Cable and Y. Tsunoda, Magnetic moments and short-range order in CoMn and NiMn alloys, J. Magn. Magn. Mater. **140**, 93 (1995).

[52] S. Kokado, N. Fujima, K. Harigaya, H. Shimizu, and A. Sakuma, Theoretical analysis of highly spin-polarized transport in the iron nitride Fe_4N, Phys. Rev. B **73**, 172410 (2006).

[53] Y. Imai, Y. Takahashi, and T. Kumagai, Relations of electronic energies and magnetic moments of tetra-3d metal (Mn, Fe, Co and Ni) nitrides calculated using a plane-wave basis method, J. Magn. Magn. Mater. **322**, 2665 (2010).

[54] S. V. Karthik, T. M. Nakatani, A. Rajanikanth, Y. K. Takahashi, and K. Hono, Spin polarization of CoFe alloys estimated by point contact Andreev reflection and tunneling magnetoresistance, J. Appl. Phys. **105**, 07C916 (2009).

[55] J. C. Tung and G. Y. Guo, High spin polarization of the anomalous Hall current in Co-based Heusler compounds, New J. Phys. **15**, 033014 (2013).

[56] T. Taniguchi, J. Grollier, and M. D. Stiles, Spin-Transfer Torques Generated by the Anomalous Hall Effect and Anisotropic Magnetoresistance, Phys. Rev. Appl. **3**, 044001 (2015).

[57] Y. Miura and K. Masuda, First-principles calculations on the spin anomalous Hall effect of ferromagnetic alloys, Phys. Rev. Mater. **5**, L101402 (2021).

[58] S. Iihama, T. Taniguchi, K. Yakushiji, A. Fukushima, Y. Shiota, S. Tsunegi, R. Hiramatsu, S. Yuasa, Y. Suzuki, and H. Kubota, Spin-transfer torque induced by the spin anomalous Hall effect, Nat. Electron. **1**, 120 (2018).

[59] J. D. Gibbons, D. MacNeill, R. A. Buhrman, and D. C. Ralph, Reorientable Spin Direction for Spin Current Produced by the Anomalous Hall Effect, Phys. Rev. Appl. **9**, 064033 (2018).

[60] A. Bose, D. D. Lam, S. Bhuktare, S. Dutta, H. Singh, Y. Jibiki, M. Goto, S. Miwa, and A. A. Tulapurkar, Observation of Anomalous Spin Torque Generated by a Ferromagnet, Phys. Rev. Appl. **9**, 064026 (2018).

[61] T. Seki, S. Iihama, T. Taniguchi, and K. Takanashi, Large spin anomalous Hall effect in $L1_0$-FePt: Symmetry and magnetization switching, Phys. Rev. B **100**, 144427 (2019).